

NEW X-RAY OBSERVATIONS OF THE GEMINGA PULSAR WIND NEBULA

GEORGE G. PAVLOV¹, SUDIP BHATTACHARYYA², AND VYACHESLAV E. ZAVLIN³

Draft version November 2, 2018

ABSTRACT

Previous observations of the middle-aged pulsar Geminga with *XMM-Newton* and *Chandra* have shown an unusual pulsar wind nebula (PWN), with a 20'' long central (axial) tail directed opposite to the pulsar's proper motion and two 2' long, bent lateral (outer) tails. Here we report on a deeper *Chandra* observation (78 ks exposure) and a few additional *XMM-Newton* observations of the Geminga PWN. The new *Chandra* observation has shown that the axial tail, which includes up to three brighter blobs, extends at least 50'' (i.e., $0.06d_{250}$ pc) from the pulsar (d_{250} is the distance scaled to 250 pc). It also allowed us to image the patchy outer tails and the emission in the immediate vicinity of the pulsar with high resolution. The PWN luminosity, $L_{0.3-8\text{keV}} \sim 3 \times 10^{29} d_{250}^2 \text{ erg s}^{-1}$, is lower than the pulsar's magnetospheric luminosity by a factor of 10. The spectra of the PWN elements are rather hard (photon index $\Gamma \sim 1$). Comparing the two *Chandra* images, we found evidence of PWN variability, including possible motion of the blobs along the axial tail. The X-ray PWN is the synchrotron radiation from relativistic particles of the pulsar wind; its morphology is connected with the supersonic motion of Geminga. We speculate that the outer tails are either (1) a sky projection of the limb-brightened boundary of a shell formed in the region of contact discontinuity, where the wind bulk flow is decelerated by shear instability, or (2) polar outflows from the pulsar bent by the ram pressure from the ISM. In the former case, the axial tail may be a jet emanating along the pulsar's spin axis, perhaps aligned with the direction of motion. In the latter case, the axial tail may be the shocked pulsar wind collimated by the ram pressure.

Subject headings: pulsars: individual (Geminga) — stars: neutron — stars: winds, outflows — X-rays: stars

1. INTRODUCTION

Pulsars lose their spin energy via relativistic pulsar winds (PWs) of charged particles. The PW shocks in the ambient medium and forms a pulsar wind nebula (PWN) whose synchrotron radiation can be observed in a very broad energy range, from the radio to TeV γ -rays (see Kaspi et al. 2006, Gaensler & Slane 2006, and Kargaltsev & Pavlov 2008 [KP08 hereafter] for recent reviews). The shocked PW is confined between the termination shock (TS) and contact discontinuity (CD) surface that separates the shocked PW from the shocked ambient medium between the CD and the forward shock (FS). The shapes of the TS, CD, and FS depend on the wind outflow geometry and the ratio of the pulsar's speed to the sound speed in the ambient medium (the Mach number), $\mathcal{M} = v_{\text{psr}}/c_s$. In particular, if the pulsar moves with a supersonic speed, $\mathcal{M} \gg 1$, and the preshock PW is isotropic, then the TS, CD, and FS acquire bow-like shapes ahead of the pulsar, with the TS apex ("head") at a distance $R_{\text{TS,h}} \approx (\dot{E}/4\pi c p_{\text{ram}})^{1/2}$, where $p_{\text{ram}} = \rho_{\text{amb}} v_{\text{psr}}^2$ is the ram pressure, ρ_{amb} the density of the ambient medium (e.g., Bucciantini et al. 2005; hereafter B+05). The shocked PW forms a tail behind the pulsar, with a flow speed significantly exceeding the pulsar's speed (Romanova et al. 2005; B+05).

Among ~ 60 PWNe detected by *Chandra*, about 20

PWNe show such bowshock-tail morphologies (KP08). Such tails have been observed, for instance, behind the pulsars J1747–2958 (Gaensler et al. 2004), J1509–5850 (Kargaltsev et al. 2008), B0355+54 (McGowan et al. 2006), and B1929+10 (Misanovic et al. 2008), with very different spindown ages, $\tau_{\text{sd}} \equiv P/(2\dot{P}) = 26, 160, 620$, and 3100 kyr, respectively. We should note, however, that the detailed shape of the detected bowshock-tail PWNe is often different from the idealized models, especially in the immediate vicinity of the pulsar, possibly because of anisotropies of the pulsar outflows. For instance, by analogy with a few bright, well-resolved PWNe around young pulsars moving with subsonic velocities (such as the Crab PWN; Weisskopf et al. 2000), one can expect that the pulsar outflows consist of equatorial and axial components, with respect to the spin axis, which are responsible for the "tori" and "jets" observed in these torus-jet PWNe (KP08).

One of the most peculiar PWNe has been detected around the famous Geminga pulsar (PSR J0633+1746). Geminga was discovered as a γ -ray source $\gamma 195+5$, with the SAS-2 satellite (e.g., Thompson et al. 1977). The period of Geminga, $P = 237$ ms, was discovered by Halpern & Holt (1992) in X-ray observations with the *Röntgen Satellit (ROSAT)*, and the period derivative, $\dot{P} = 1.1 \times 10^{-14} \text{ s s}^{-1}$, was first measured by Bertsch et al. (1992) in γ -rays with the *Compton Gamma Ray Observatory (CGRO)*. The period and its derivative correspond to the spindown age $\tau_{\text{sd}} = 340$ kyr and spindown power $\dot{E} = 3.3 \times 10^{34} \text{ erg s}^{-1}$. The Geminga pulsar has also been detected in the optical (Halpern & Tytler 1988; Bignami et al. 1988), near-IR (Kopt-

¹ Pennsylvania State University, 525 Davey Lab., University Park, PA 16802; pavlov@astro.psu.edu

² Department of Astronomy and Astrophysics, Tata Institute of Fundamental Research, Mumbai 400005, India; sudip@tifr.res.in

³ USRA/NASA MSFC Space Science Office, Huntsville, AL 35812; vyacheslav.zavlin@msfc.nasa.gov

sevich et al. 2001), and UV (Kargaltsev et al. 2005). The distance to Geminga, $d = 250_{-62}^{+120}$ pc, was estimated from its annual parallax measured in observations with the *Hubble Space Telescope* (Faherty et al. 2007). Its proper motion, 178.2 ± 1.8 mas/yr, corresponds to the transverse velocity, $v_{\perp} \approx 211d_{250}$ km s⁻¹ [where $d_{250} = d/(250 \text{ pc})$]. As this velocity considerably exceeds the typical sound speed in the interstellar medium (ISM), $c_s \sim 10\text{--}30$ km s⁻¹, one should expect Geminga to be accompanied by a bowshock-tail PWN, with $R_{\text{TS,h}} = 1.1 \times 10^{16} n^{-1/2} (d_{250}/\sin i)^{-1}$ cm, which corresponds to $\approx 2.9'' n^{-1/2} (d_{250}/\sin i)^{-2}$, where i is the angle between the pulsar's velocity and the line of sight, and $n = \rho_{\text{amb}}/m_{\text{H}}$.

XMM-Newton observations of Geminga in 2002 April, reported by Caraveo et al. (2003; hereafter C+03), revealed two $\approx 2'$ long tails behind the pulsar, approximately symmetric with respect to the sky projection of the pulsar's trajectory (see Fig. 1), with a luminosity of $\sim 10^{29}$ erg s⁻¹ in the 0.3–5 keV band. C+03 suggested that these tails are associated with a bowshock generated by the pulsar's motion, and, using the one-zone bowshock model by Wilkin (1996)⁴, predicted that the head of the bowshock, $20''\text{--}30''$ ahead of the pulsar, is hidden in the bright wings of the pulsar point spread function (PSF) in the *XMM-Newton* image.

The Geminga field was observed in 2004 (Sanwal et al. 2004; Pavlov et al. 2006 [hereafter P+06]) with the *Chandra* Advanced CCD Imaging Spectrometer (ACIS), whose resolution, $\approx 0''.5$, is much better than that of the *XMM-Newton* detectors. The most interesting finding of that observation was the detection of an axial tail behind the pulsar aligned with the direction of the pulsar's proper motion (P+06; de Luca et al. 2006; see Fig. 2, top). The axial tail, with a luminosity $\sim 2 \times 10^{29} d_{250}^2$ erg s⁻¹, was seen up to $25''$ from the pulsar, almost up to the boundary of the field of view (FOV). P+06 suggested that the axial tail may be a jet emanating from the pulsar magnetosphere. In addition to the axial tail, a faint arc-like structure was detected $5''\text{--}7''$ ahead of the pulsar (but no emission at $20''\text{--}30''$, contrary to the C+03 prediction), and a 3σ enhancement, apparently connecting the arc with one of the outer tails (south of the axial tail), was noticed (P+06). No emission was detected from the other (northern) outer tail in that short, ≈ 20 ks, exposure.

To image the whole extent of the Geminga PWN and study its tails in more detail, we observed this field with *Chandra* ACIS in 2007, with a longer exposure and a larger FOV. In this paper, we report the results of this observation and compare them with the previous findings. We describe the data analysis and the observational results in § 2, and discuss the implications of these results in § 3.

⁴ The one-zone model assumes an instant mixing of the PW matter with the ambient matter at the shock, so that there is no CD, and the TS and FS suraces coincide with each other. The numerical bowshock models (e.g., Bucciantini 2002) have shown that the shape of the one-zone shock is approximately similar to that of the FS but very different from the TS shape.

2. DATA ANALYSIS AND RESULTS

2.1. Observations and data reduction

The Geminga field was observed with *Chandra* ACIS on 2007 August 27 for 78.12 ks (ObsID 7592). The observation was taken in Timed Exposure (TE) mode, with the frame time of 3.24 s. After removing 20 s of high background and correcting for the detector dead time, the scientific exposure time (live time) is 77,077 s. To maximize the signal-to-noise ratio (S/N) for the very faint PWN emission, we imaged the field onto the front-illuminated I3 chip, which has a lower background than the commonly used (and slightly more sensitive) back-illuminated S3 chip⁵. We used the Very Faint telemetry format to provide a better screening of background events⁶. As putting the target at the ACIS-I aimpoint (near the corner of the I3 chip) could result in chip gaps crossing the PWN image, we moved the focus to the middle of node 2 on the I3 chip (SIM-Z = -7.42 mm = $-2'.53$) and applied the $\Delta Y = -1'.6$ offset to put the pulsar at $\gtrsim 2'$ from the chip boundaries.

To obtain a deeper PWN image and examine a possible PWN variability, we also used the previous *Chandra* observation of Geminga carried out on 2004 February 7 (ObsID 4674; 18,793 s scientific exposure). The details of that observation have been described by P+06. Here we only mention that the observation was taken in Faint telemetry format, and the Geminga pulsar and its PWN were imaged on 1/8 subarray of the S3 chip ($\approx 1' \times 8'$ FOV), which reduced the pileup in the pulsar image but did not allow us to image the whole PWN.

We have used the *Chandra* Interactive Analysis of Observations (CIAO) software (ver. 4.0; CALDB ver. 3.4.0) for the ACIS data analysis, starting from the level 1 event files. We have applied the standard grade filtering and used the energy range 0.3–8 keV to minimize the background contribution. We have also applied the exposure map correction, but found that the effects of nonuniform exposure and nonuniform CCD response in the PWN region are small (except for the boundary of the 1/8 subarray used in the observation of 2004).

To confront the high-resolution *Chandra* data with the *XMM-Newton* results, we also used the data obtained with the MOS1 and MOS2 detectors of the European Photon Imaging Camera (EPIC) on board *XMM-Newton*. In addition to the observation of 2002 April 4–5 (ObsID 011117010; 77.97 ks scientific exposure, after removing the periods of high background) reported by C+03 and P+06, we also used the data sets obtained in observations 0201350101 of 2004 March 13 (16.23 ks scientific exposure), 031159100 of 2006 March 17 (4.46 ks), 0400260201, 2006 October 2 (19.70 ks), and 0400260301 of 2007 March 11 (23.83 ks). The total effective exposure of the five observations is 142.18 ks. All the observations were taken with medium filter in Full Frame mode, providing a $30'$ diameter FOV. The data reduction was performed with the Scientific Analysis System (SAS) package (ver. 8.0.0). Good events with patterns 0–12 and energies within the 0.3–8 keV range were selected for the data analysis.

⁵ See § 6.16 of The *Chandra* Proposers' Observatory Guide (POG), <http://asc.harvard.edu/proposer/POG>.

⁶ See § 6.14 of the *Chandra* POG.

2.2. Images and spectra of the PWN elements

The *Chandra* ACIS data of 2007 provide the high-resolution image of the entire Geminga PWN for the first time (see the top panel of Fig. 2 and Fig. 3). Below we will describe the observed properties of the PWN elements, and compare them with the results of the 2004 ACIS observation.

To calculate the net source counts N_S in the area A_S of a PWN element, we use the formula $N_S = N_T - (A_S/A_B)N_B$, where N_T is the total number of counts detected from the area A_S , and N_B is the number of background counts detected from the area A_B . Then the 1σ error of N_S and the signal-to-noise ratio are given by $\delta N_S = [N_S + (1 + A_S/A_B)(A_S/A_B)N_B]^{1/2}$ and $S/N = N_S/\delta N_S$, respectively.

For the analysis of the 2004 data, we use a source-free rectangular background region ($A_B = 3439$ arcsec², $N_B = 129$ counts in the 0.3–8 keV band) to the north of the Geminga pulsar. For the 2007 data, we use the background measured from a source-free rectangular region, with the area $A_B = 5399$ arcsec², in the northeast portion of the ACIS-I3 chip (unless stated otherwise). This region contains $N_B = 416$ counts in the 0.3–8 keV band, which corresponds to the background brightness of 1.0×10^{-6} counts arcsec⁻² s⁻¹, a factor of 2 lower than in the *Chandra* observation of 2004. The values of N_S and S/N for the PWN elements are given in Table 1.

For the spectral analysis, we have used the XSPEC package (ver. 12.4.0) and fit the spectra with the absorbed power-law (PL) model (`wabs*powerlaw`), with the fixed hydrogen column density $N_H = 1.1 \times 10^{20}$ cm⁻² (Halpern & Wang 1997; de Luca et al. 2005). As the number of counts in the PWN is small, we use the maximum likelihood method (C-statistic) for spectral fitting. Table 1 provides the values of the photon index Γ and the flux F of the PWN elements.

2.2.1. Axial tail

The brightest feature of the Geminga PWN in the *Chandra* data of 2004 is the axial tail (A-tail hereafter), seen up to at least 25'' from the pulsar in the direction opposite to the pulsar's proper motion (see P+06 and Fig. 2, middle). In the image from the 2007 observation, we see the A-tail up to at least 50'' (0.06 d_{250} pc) from the pulsar (Fig. 2, top), with 83 ± 12 source counts within the region of 706 arcsec² area shown by the solid lines in Figure 3. The PL fit of its spectrum (see Table 1 and Fig. 4) gives the photon index $\Gamma = 1.8 \pm 0.3$ and the 0.3–8 keV luminosity $L = (0.9 \pm 0.1) \times 10^{29}$ erg s⁻¹ (assuming an isotropic emission at $d = 250$ pc), versus $\Gamma = 1.3 \pm 0.3$ and $L = (1.6 \pm 0.3) \times 10^{29}$ erg s⁻¹ in the 2004 data, as measured in the 118 arcsec² area rectangle that contains 46 ± 7 counts (shown in the middle panel of Fig. 2).

The A-tail looks patchy in both the 2004 and 2007 observations, with some ‘‘blobs’’ standing out. The blobs, labeled A, B, and C in Figure 2 are at the distances of about 9'', 20'', and 43'' from the pulsar, respectively (blob A is seen in the 2004 image, while blob B and blob C are seen in the 2007 image). They contain 24.9 ± 5.1 , 12.8 ± 3.9 , and 25.8 ± 5.3 source counts, respectively, within the 3''-radius circles around their centers. The analysis of the brightness distribution along the A-tail shows that the blobs are significant at $> 3\sigma$ levels (i.e.,

they are not just statistical fluctuations of the brightness distributions). For instance, the number of counts in the 2'' radius circle around the center of blob B (15 counts) exceeds the average number of counts per the same 12.6 arcsec² area in the A-tail (2.44 ± 0.21 counts) at the 3.2σ level. The nonuniform surface brightness distribution along the A-tail, and the difference of these distributions in the 2004 and 2007 images are shown in Figure 5.

The brightest in the 2007 data is blob C at the apparent end of the tail, centered at $\alpha = 06^{\text{h}}33^{\text{m}}51^{\text{s}}.71$, $\delta = +17^{\circ}45'53''.1$ (J2000). Because of the small number of counts, we cannot firmly determine whether the blob corresponds to a point source or an extended one. Interestingly, the end portion of the tail looks attached to this blob, while the tail looks detached from the pulsar in both the 2004 and 2007 images. Therefore, one could even speculate that the tail might belong not to Geminga but to some unrelated field object (e.g., it might be a jet of an active galactic nucleus [AGN], accidentally oriented toward Geminga in the sky projection).

To check whether the blobs are indeed associated with the tail or they may be background sources, we examined the optical/NIR catalogs. We found no optical counterparts to blob A and blob B, but we found an object at $\alpha = 06^{\text{h}}33^{\text{m}}51^{\text{s}}.69$, $\delta = +17^{\circ}45'54''.2$ (J2000), about 1'' from the center of blob C (the coordinates are from the USNO-B1.0 catalog [Monet et al. 2003], with the quoted mean uncertainties of 0''.075 and 0''.094 in α and δ , respectively). Based on the magnitudes and colors (e.g., $V = 17.7 \pm 0.3$ [GSC2.3 catalog; Lasker et al. 2008], $J = 16.18 \pm 0.09$, $H = 15.54 \pm 0.11$, $K = 15.6 \pm 0.2$ [2MASS catalog; Cutri et al. 2003]), this object could be a background K star. Such a star could contribute to the X-ray emission of blob C. The observed X-ray flux in the 3'' radius aperture is $F_{0.3-3.5 \text{ keV}} \approx 3.8 \times 10^{-15}$ erg cm⁻² s⁻¹. According to Maccararo et al. (1988), the X-ray/optical flux ratio, $\log(F_{0.3-3.5 \text{ keV}}/F_V) \approx -2.0$, corresponds to a K or M star, and it excludes an AGN [for which $-1.2 < \log(F_{0.3-3.5 \text{ keV}}/F_V) < +1.6$] as the source of the X-ray and optical emission (hence the tail is not an AGN jet). Thus, we cannot rule out the possibility that a K star, accidentally projected onto the A-tail, is at least partly responsible for the brightened end of the tail in the 2007 image. However, if we exclude blob C, the tail's luminosity decreases by a factor of 1.5, but the spectral slope remains virtually the same (see Table 1 and Fig. 4). This suggests that the star's contribution does not dominate in the blob C emission, but, because of the small number of counts and large statistical errors, we cannot firmly conclude on the nature of blob C.

In the observation of 2004, blob C was imaged onto an underexposed part of the FOV (because of the dither), between the dashed lines in the middle panel of Figure 2. Taking into account the shorter effective exposure of that observation (but the higher sensitivity of the S3 chip), we expect 4.2 ± 2.1 counts to be detected in the 2'' radius circle around the position of the blob C centroid; however, there are no counts within that circle. This may suggest some variability of the source, but the statistical significance of this difference is marginal (e.g., the probability of detecting zero counts when 4.2 counts are expected is 0.0145, which corresponds to a 2.4σ significance).

Based on the ACIS count rate of blob C in 2007, one

could expect to detect about 90 counts in the $15''$ radius aperture in the 142 ks MOS1+MOS2 exposure, but we found only 49 ± 12 counts in the MOS data. Furthermore, we note that the blob C position is projected onto the wings of the pulsar PSF in the *XMM-Newton* images (see Fig. 1), whose contribution to the number of extracted counts is difficult to evaluate because of the “spiky” shape of the PSF. Anyway, the number of counts expected for blob C in the *XMM-Newton* data significantly exceeds the measured one, suggesting variability of blob C.

The A-tail images (Fig. 2) look appreciably different in the 2004 and 2007 data, in both the overall flux and the surface brightness distribution (see Fig. 5). For instance, the flux, 2.2×10^{-14} erg cm $^{-2}$ s $^{-1}$, in the 118 arcsec 2 area of the tail in the 2004 data is a factor of 6 higher than the flux from the same area in the 2007 data (the difference between the count rates is significant at the 5σ level, with account for a factor of 1.6 higher sensitivity of the S3 chip compared to that of the I3 chip, for $\Gamma = 1.8$ and $N_H = 1.1 \times 10^{20}$ cm $^{-2}$).

The different positions of the blobs in the 2004 and 2007 images suggest that the blobs are moving along the A-tail (perhaps similar to the blobs in the Vela pulsar jet; Pavlov et al. 2003). One might even speculate that, for instance, blob B is, in fact, blob A that had moved $11''$ (4×10^{16} d_{250} cm) in 3.5 yr between the observations (which would correspond to the transverse velocity of $v_{\text{blob},\perp} \sim 3700 d_{250}$ km s $^{-1}$). However, as blob B could also form independently after the disappearance of blob A, this will remain a speculation until the characteristic blob lifetime is estimated in a series of monitoring observations.

In the large-scale *Chandra* image of 2007 (Fig. 3), one can see a possible faint extension of the A-tail (within the dashed polygon in Fig. 3). This faint portion has a factor of 1.5 higher observed flux (but a factor of 2.4 lower average brightness) than the bright portion (see Table 1). However, its statistical significance is only 1.7σ , and it is not seen in the deep *XMM-Newton* image (see Fig. 1). Therefore, this “faint portion” most likely represents a string of background fluctuations accidentally aligned in the A-tail direction.

2.2.2. Outer tails

The two “outer tails” of the Geminga PWN, seen up to $\sim 2'$ from the pulsar, were originally detected in the *XMM-Newton* observations of 2002 April (C+03). Adding four shorter observations of 2004–2007, which increases the total exposure by a factor of 1.8, shows qualitatively the same picture (Fig. 1). The two tails are approximately symmetric with respect to the pulsar’s trajectory in the sky, forming a horseshoe-like structure. The southern and northern tails (we will call them the S-tail and N-tail, for brevity) are seen up to $3'1$ and $2'7$ from the pulsar, respectively, in the summed MOS1+MOS2 image. Their typical width, $\sim 20''$ – $30''$, is comparable to the *XMM-Newton* angular resolution. The tails in the pulsar vicinity (within $\approx 30''$) are immersed in the bright pulsar’s image. The spectrum of the combined emission from the two tails, extracted from the $120'' \times 40''$ elliptical regions shown in Figure 1 (about 560 source counts), can be described by a PL model with $\Gamma = 1.7 \pm 0.2$ ($\chi^2_\nu = 1.36$ for 50 degrees of freedom [d.o.f.],

for fixed $N_H = 1.1 \times 10^{20}$ cm $^{-2}$). The unabsorbed flux and luminosity of the two tails, are $F^{\text{unabs}} \simeq 1.7 \times 10^{-14}$ erg cm $^{-2}$ s $^{-1}$ and $L \simeq 1.3 \times 10^{29} d_{250}^2$ erg s $^{-1}$, in the 0.3–8 keV band. Both the total flux and the spectral slope are consistent with those obtained by C+03. The contribution of the S-tail into the total energy flux is about 76%. The average specific intensities in the S-tail and N-tail elliptical regions are 3.4×10^{-18} and 1.1×10^{-18} erg cm $^{-2}$ s $^{-1}$ arcsec $^{-2}$, respectively. Fitting the spectra of the S-tail and N-tail separately, we obtained $\Gamma = 1.4 \pm 0.3$ and 2.7 ± 1.1 , respectively. The apparently large difference between the spectral slopes, $\Delta\Gamma = 1.3 \pm 1.1$, is not statistically significant. The spectra can also be fitted by the models for emission of an optically thin thermal plasma (e.g. $kT = 8_{-3}^{+10}$ keV for the fit of the S-tail + N-tail spectrum with the *mekal* model; $\chi^2_\nu = 1.36$ for 50 d.o.f.).

Thanks to its high angular resolution, *Chandra* observations make it possible to image the tails in the pulsar vicinity and resolve the tail structure. In the short observation of 2004 the N-tail was not detected, while the initial portion of the S-tail was detected with about 3σ significance (P+06). The entire extent of the tails could not be seen because the $1/8$ subarray was used.

In the *Chandra* data of 2007 we have detected both outer tails. For the analysis, we divide each of the tails into two parts. The bright initial parts (up to $2'$ and $40''$ from the pulsar, for the S-tail and N-tail, respectively) are delineated by solid polygons in Figure 3, while the longer faint parts (up to $4'2$ and $3'6$ from the pulsar, respectively) are shown by dashed polygons. (We note that the bright portion of the N-tail and a substantial part of the bright portion of the S-tail are hidden behind the pulsar image in the *XMM-Newton* data.) The statistical significance of the faint parts is marginal in the *Chandra* data (see Table 1), but their reality is supported by the *XMM-Newton* data (see Fig. 6, where the *XMM-Newton* brightness contours are overlaid on the *Chandra* image). The end parts of the S-tail in the *Chandra* and *XMM-Newton* images are slightly shifted with respect to each other, which might suggest possible variability of the outer tails. The *Chandra* image resolves the tails in the transverse dimension, showing $\gtrsim 20''$ widths, but the image is not deep enough to infer the brightness distribution across the tails. Also, the tails do not show sharp-cut outer boundaries, perhaps because of the same reason.

Figure 6 also shows the locations of four optical-NIR sources that are projected onto the tails. We have already discussed one of them (#1 in Fig. 6, whose position coincides with blob C in the A-tail). The other three sources (numbered 2, 3, and 4 in Fig. 6, with V magnitudes of 17.6, 15.3, and 13.4, respectively, from the NOMAD catalog; Zacharias et al. 2004) are projected onto the S-tail. Source 3 and source 4 are likely an F star and a K star, respectively, based on their optical-NIR colors, while the magnitude errors for the fainter source 2 are too large to determine its nature. The $2.55''$ radius circles around the positions of the sources 2, 3, and 4 contain 7, 1, and 11 counts, respectively. Even if the X-ray emission at these locations is due to the optical sources, the total number of detected source counts from all the three sources (assuming they are pointlike) is only 14.3 ± 4.4 , while the number of counts from the entire S-

tail is 168 ± 34 (Table 1). Therefore, their contribution to the observed X-ray emission from the entire S-tail is negligible.

The PL fits of the outer tails’ spectra (see Table 1 and Fig. 4) indicate that the spectral slope of the S-tail does not differ significantly from that of the A-tail (e.g., $\Gamma \approx 1.5$ fits both spectra within the 1σ uncertainties), while the N-tail is apparently harder, in contradiction to the result found from the *XMM-Newton* data. Although the observed number of counts from the N-tail is a factor of 1.8 lower than that from the S-tail, their luminosities are comparable. Table 1 also suggests that both the N-tail and S-tail spectra soften from the bright parts toward the extended faint portions, but the statistical significance of the softening is low (e.g., $\Delta\Gamma \approx 0.7 \pm 0.5$ for the S-tail). The total luminosity of the two tails is $L \approx 4.2 \times 10^{29} d_{250}^2 \text{ erg s}^{-1}$, in the 0.3–8 keV band, assuming isotropic emission. This value exceeds the estimate derived above from the *XMM-Newton* data by a factor of about 3, but that estimate was obtained for a fraction of outer tails, which did not include the bright part of the N-tail and included only a small portion of the bright part of the S-tail. The average specific intensities in the bright parts are about 1.2×10^{-17} and $2.6 \times 10^{-17} \text{ erg cm}^{-2} \text{ s}^{-1} \text{ arcsec}^{-2}$, for the S-tail and N-tail, respectively.

Similar to the A-tail, the bright and faint portions of the S-tail and the faint portion of the N-tail look patchy. To quantify the statistical significance of the patchiness, we have compared the net counts from brighter and fainter regions of equal size for each of these components. For the bright S-tail, faint S-tail, and faint N-tail, we found significances of 2.5σ , 2.2σ , and 2.1σ , respectively. Therefore, the patchiness is not ruled out, but a deeper observation is required to prove it firmly. A similar analysis of the *XMM-Newton* data does not show a statistically significant patchiness, because of large noise and poor angular resolution.

To examine variability of the outer tails, we have compared the count rates in the area of 462 arcsec^2 of the bright part of the N-tail (39.4 ± 8.8 and 5.7 ± 5.0 net counts in the observations of 2007 and 2004, respectively). Accounting for the factor of 1.2 higher sensitivity of the S3 chip compared to the I3 chip (for the spectral parameters derived from the 2007 observation), the difference between the count rates is significant at the 3.5σ level. On the other hand, the difference of the count rates in the 985 arcsec^2 area of the bright part of the S-tail, which was detected in both the 2004 and 2007 *Chandra* observations (33.0 ± 9.0 and 79.1 ± 13.0 net counts, respectively), is statistically insignificant. We have also looked for variability of the outer tails in the *XMM-Newton* data, but found no statistically significant differences between the separate observations because of the strong noise.

As it is natural to assume that the “outer tails” represent the sky projection of limb-brightened boundaries of a shell, one can expect some X-ray emission from the region between the outer tails, in addition to the A-tail. To look for this emission, we have inspected two inter-tail regions of combined area $A_S = 12,898 \text{ arcsec}^2$ that exclude the entire (bright plus faint) A-tail and contain $N_T = 886$ counts. Using the background extracted from three source-free rectangles around the PWN ($N_B = 2222$ counts in the combined area $A_B = 29,578 \text{ arcsec}^2$), we

found $N_S = -88 \pm 36$ net counts from the “source”. Adding the alleged faint portion of the A-tail, which gives $N_T = 1101$ counts in the area $A_S = 15,302 \text{ arcsec}^2$, we found $N_S = -48 \pm 41$ net counts. Thus, we conclude that there is no detectable emission from the region between the outer tails, and the “faint portion” of the A-tail is likely an illusion (in agreement with our conclusion at the end of § 2.2.1). Using the approach outlined by Weisskopf et al. (2007), we find the 3σ upper limit of 94 counts in the area $A_S = 15,302 \text{ arcsec}^2$ (99% and 90% upper limits are 78 and 45 respectively). The corresponding 3σ upper limit on the surface brightness, $6.1 \times 10^{-3} \text{ counts arcsec}^{-2}$, is lower than the average surface brightness of the outer tails (e.g., by factors of 4.6 ± 0.9 and 3.4 ± 1.0 for the “entire” S-tail and N-tail, respectively).

The *XMM-Newton* image also does not show detectable inter-tail emission. Using the same approach, we found the 3σ upper limit of 37 counts in the $32'' \times 64''$ box between the outer tails shown in Figure 1 (99% and 90% upper limits are 32 and 22 counts, respectively). The corresponding 3σ upper limit on surface brightness, $1.8 \times 10^{-2} \text{ counts arcsec}^{-2}$, is lower by factors of 6.2 ± 0.2 and 2.0 ± 0.4 than the surface brightnesses of the S-tail and N-tail, respectively.

2.2.3. Emission ahead of the pulsar

An arc-like diffuse emission region, about $5''$ – $7''$ ahead of the pulsar, was reported by P+06 from the 2004 *Chandra* data. We have analyzed the data inside a polygon (area = 86.6 arcsec^2) and found 22.8 ± 5.1 source counts. Our spectral analysis provides a photon index $\Gamma = 0.9 \pm 0.5$ and the observed flux $F \approx 1.2 \times 10^{-14} \text{ erg cm}^{-2} \text{ s}^{-1}$, in the 0.3–8 keV band, consistent with the P+06 estimates.

Based on these results, the expected number of arc counts in the *Chandra* observation of 2007⁷ is 83 ± 24 . However, although some diffuse emission is seen at that site in the 2007 data, there are only 16.3 ± 4.8 source counts in the corresponding polygon (at the same distance from the pulsar, which has moved $0''.62$ in the sky in the 3.5 years), and the shape of the count distribution does not resemble an arc (see the upper panel of Fig. 2). The spectral slope, $\Gamma = 1.1 \pm 0.7$, is consistent with that of the 2004 arc, but the observed flux, $F \approx 2.5 \times 10^{-15} \text{ erg cm}^{-2} \text{ s}^{-1}$, is a factor of 5 lower. This suggests that the emission ahead of the pulsar is variable, but the significance of this variability is not very high (e.g., 2.8σ in the difference between the expected and observed counts).

The alleged arc cannot be seen in the *XMM-Newton* images because it is hidden in the pulsar PSF. However, these images show a “streak” ahead of the pulsar, in the direction of the proper motion, which is best seen in the summed image (bottom panels of Fig. 1). One might speculate that this streak is a Geminga PWN element (e.g., a forward jet). To check this hypothesis, we extracted 760 source counts from the $20'' \times 50''$ rectangle that includes the streak (shown in the bottom panels of Fig. 1) and fit the spectrum with various models. We found that the very soft streak spectrum does not fit the PL model ($\chi^2_\nu = 4.3$ for 44 d.o.f.), but it fits the two-component PL+blackbody model ($\Gamma = 1.8 \pm 0.1$,

⁷ Estimated with the aid of the *Chandra* PIMMS tool; <http://asc.harvard.edu/toolkit/pimms.jsp>

$kT = 0.53 \pm 0.05$ keV, $\chi^2_\nu = 1.1$ for 42 d.o.f.) that is consistent with the pulsar’s spectrum (e.g., Kargaltsev et al. 2005). Therefore, we conclude that the streak is not related to the PWN, but it is an artificial spike-like feature in the MOS PSF caused by the “spiders” holding the X-ray telescopes (see the XMM-Newton Users’ Handbook, Sec. 3.2.1.1) This conclusion is also supported by a lack of any excess above the background at the corresponding area in the *Chandra* images.

Interestingly, the summed 2004 + 2007 *Chandra* image in the bottom panel of Figure 2 shows a hint of a short, $10''$ – $15''$, jetlike structure ahead of the pulsar, with its end seemingly connecting to the N-tail. The number of counts is, however, too small to conclude whether this structure is an accidentally aligned superposition of events from the two images or there is indeed a forward jet, perhaps bent in the north-northwest direction into the N-tail, which we cannot see in the separate images because of the scarce statistics. A deeper observation is needed to understand the true nature of this and other apparent structures in the immediate vicinity of the pulsar.

3. DISCUSSION

The *Chandra* observation of 2007 has confirmed the existence of three tail-like features in the Geminga PWN image, with comparable luminosities, and allowed us to study the PWN in more detail (e.g., to detect the A-tail at larger distances from the pulsar and investigate the PWN in the immediate vicinity of the pulsar). Moreover, it has provided first evidence of variability of the PWN elements, in particular, of the A-tail and the emission in the pulsar vicinity.

The observed structure of the Geminga PWN looks very unusual. Although the overall appearance of the PWN, particularly the alignment of the tails with the pulsar’s proper motion, leaves no doubts that the PWN structure is caused by the supersonic motion of the pulsar in the ISM, none of the other ~ 20 bowshock-tail PWNe detected by *Chandra* (see KP08) show three distinct tails. To interpret the observed structure in terms of the PWN models, we should first understand the intrinsic three-dimensional morphology of the X-ray PWN, which is by no means obvious.

At the first glance, the most natural interpretation of the PWN elements is that the “outer tails”, together with the “arc” that apparently connects the tails ahead of the pulsar, delineate the limb-brightened boundary of the sky projection of an optically thin shell, shaped approximately as a paraboloid of revolution, while the nearly straight axial tail represents a collimated outflow in the direction opposite to that of the pulsar’s motion. On the other hand, one cannot exclude the possibility that the outer tails are, in fact, hose-like structures, such as jets confined by their own magnetic fields and bent by the head wind of ISM matter. Moreover, one could even speculate that the axial “tail” is Doppler-boosted emission from a narrow region of a shell formed by material flowing with relativistic speeds. Below we will discuss these possibilities in more detail.

3.1. Possible interpretations of the outer tails

The patchy outer tails of $20''$ – $30''$ width are seen up to $\sim 3'$ ($\sim 0.2d_{250}$ pc) from the pulsar. Their X-ray lumi-

osity, $L_X \sim 4 \times 10^{29} d_{250}^2 \text{ erg s}^{-1}$ in the 0.3–8 keV band, is a fraction of $\sim 1.2 \times 10^{-5} d_{250}^2$ of the pulsar’s spin-down power \dot{E} , lower than the typical $L_X/\dot{E} \sim 10^{-4}$ – 10^{-3} for younger PWNe (KP08). The outer tails’ luminosity is a factor of ~ 7 lower than the pulsar’s magnetospheric luminosity, while the PWN luminosity is usually higher than the magnetospheric luminosity for younger pulsars (Kargaltsev et al. 2007). The spectrum of the outer tails can be described by the absorbed PL model with $\Gamma \sim 1$, which is apparently harder than the typical PWN spectra. The explanation of the outer tails’ properties depends on the topology of the PW outflow.

3.1.1. The outer tails are shell boundaries?

Let us assume that the outer tails are limb-brightened shell boundaries and explore the consequences of this assumption. First of all, the very fact that the shell boundaries are much brighter than the rest of the shell image (see § 2.2.2) implies a nonrelativistic speed of the bulk outflow along the shell. If it were relativistic, then, due to the Doppler boosting, the brightest parts of the shell image would be not the boundaries but they would correspond to the smallest angles between the flow velocity and the line of sight. This inference restricts the number of possible interpretations of the shell. For instance, the shell cannot be interpreted as synchrotron emission from the shocked PW immediately outside the (bullet-like) TS surface – not only because the cylindrical radius of the shell is too large (see P+06), but also because the shocked PW is expected to flow with nearly relativistic speed, $v_{\text{flow}} = 0.8c$ – $0.9c$, along the lateral TS boundary (B+05). As the brightness is proportional to $[1 - (v_{\text{flow}}/c) \cos \theta]^{-\Gamma-2}$, where θ is the angle between the flow direction and the line of sight, the flow toward the observer would be a factor of $\gtrsim 100$ brighter than the flow in the perpendicular direction, for the photon index $\Gamma \approx 1$.

One might consider the possibility that the shell emission comes from the shocked ISM material heated up to X-ray temperatures. In this case, we would associate the outer tails with the FS, and the emission mechanism with the thermal emission of an optically thin plasma rather than synchrotron emission from relativistic electrons. From the junction conditions at the shock front, the expected temperature of the shocked ISM material at the head of the bowshock is $kT = (3/16)\mu m_p V_{\text{psr}}^2 = 0.078\mu V_{200}^2 \text{ keV}$ [where μ is the chemical weight, $V_{200} = V_{\text{psr}}/(200 \text{ km s}^{-1})$, and adiabatic index $\gamma_{\text{ad}} = 5/3$ is assumed for the ISM gas], and it should be even lower behind the pulsar because of the obliqueness of the shock. Since the fit of the outer tails spectrum with the `mekal` model gives $kT \approx 5$ – 18 keV (see § 2.2.2), the expected temperature of the shocked ISM gas looks too low to explain the hard spectrum of the tails emission unless $V_{\text{psr}} \gtrsim 2300\mu^{-1/2}(kT/10 \text{ keV})^{1/2} \text{ km s}^{-1}$, which would imply that the pulsar moves at a small inclination angle i with respect to the line of sight, $\sin i \lesssim 0.1$. However, since such a speed is higher than those observed for other pulsars, and the PWN appearance can hardly be reconciled with such small inclination angles, we can discard this interpretation.

It seems more reasonable to assume that the shell is formed by the shocked PW flowing immediately inside

the CD surface, where the magnetic field is compressed (B+05) and the synchrotron radiation is enhanced. However, such an interpretation contradicts the available PWN models, which predict a nearly relativistic flow speed in the outer layers of the synchrotron emitting PWN (hence dim boundaries and bright central part) because of the Doppler boosting (see above). Indeed, the simulated PWN images for $i = 90^\circ$ (see Fig. 4 in B+05) show the brightest synchrotron emission from the bowshock head region, while throughout the entire PWN the brightness decreases from the axis toward the CD, in contrast to the observed images. (This is partly caused by the assumption that the PWN magnetic field is purely toroidal, which reduces the synchrotron intensity at the PWN boundaries, where the magnetic field is parallel to the line of sight. However, even if the magnetic field is completely disordered, the brightness does not grow from the axis toward the boundaries; see Fig. 5 in B+05.) Therefore, this interpretation of the outer tails implies that there is a mechanism that decelerates the flow. The deceleration can be provided by the shear (Kelvin-Helmholtz) instabilities at the CD, which can lead to advection of clumps of the heavier shocked ISM material into the shocked PW and slow down the latter (e.g., B+05). The diffuse appearance and the patchiness of the tails in the high-resolution *Chandra* images (see §2.2.2 and Figs. 2 and 3) are consistent with this hypothesis. It could be verified observationally if the speed of the nonuniformities in the outer tails, which should form in the process of mass loading, is measured in a series of deep observations.

Another apparent problem with the interpretation of the outer tails and the arc as traces of the CD surface is the discrepancy between the observed and predicted ratios of the CD's cylindrical radius, r_{CD} , to the distance $R_{CD,h} \approx 1.3R_{TS,h}$ of the CD head from the pulsar. For instance, the B+05 model predicts $r_{CD}/R_{CD,h} \approx 3$ while the observed ratio is $\gtrsim 10 \sin i$ (if we interpret the ‘‘arc’’ ahead of the pulsar as the head of the CD surface⁸.) This means that either the inclination angle is small, $i < 15^\circ - 20^\circ$, or some assumptions of the B+05 model are violated. Since the observed PWN shape can hardly be reconciled with such small inclination angles (see Fig. 3 in C+03), we suggest that the discrepancy is caused by the assumption that the unshocked PW is isotropic. Indeed, if the wind is predominantly equatorial (i.e., concentrated around the plane perpendicular to the pulsar's spin axis), and the spin axis is aligned with the direction of pulsar motion (as observed in a number of young pulsars), then the lower wind ram pressure ahead of the pulsar should result in a smaller distance between the pulsar and the TS (and CD) apex. The only models of PWNe with anisotropic wind outflow we are aware of have been presented by Vigelius et al. (2007). These models consider only nonrelativistic flows and, more importantly, assume zero magnetic field, but they should satisfactorily describe the PWN morphology for small

⁸ If the PW is anisotropic, the head of the CD surface could be much closer to the pulsar than the observed arclike emission. In this case, the emission ahead of the pulsar could be a forward axial outflow destroyed by the ISM ram pressure. Such an outflow should be seen as a diffuse emission of an irregular, variable shape, in contrast to the CD surface head that would preserve its arclike shape and could show variations if the ISM is nonuniform.

values of the PW magnetization parameter (defined as the ratio of the Poynting flux to the kinetic energy flux). Although Vigelius et al. did not directly consider the case of an equatorial outflow perpendicular to the pulsar velocity, some of the considered cases (e.g., Fig. 6 in that paper) qualitatively confirm our explanation.

For completeness, we should also mention the interpretation suggested by C+03, that the outer tails represent the synchrotron radiation of the PW in the interstellar magnetic field ‘‘compressed in the bowshock’’ by a factor of 4 (for an adiabatic shock with $\gamma_{ad} = 5/3$ and a large Mach number), up to $\sim 10 \mu\text{G}$. As C+03 assume a one-zone shock model, which apparently does not describe realistic PWNe, this interpretation may not be directly applicable. One may speculate, however, that ultrarelativistic electrons from the high-energy tail of the electron energy distribution could leak from the shocked wind region (incide the CD) into the shocked ISM region and generate synchrotron radiation in the interstellar magnetic field amplified at the FS. We should note, however, that only the magnetic field component parallel to the shock surface is amplified by this mechanism, and the amplification becomes insignificant behind the pulsar because of the shock obliqueness. Therefore, we believe that there is no need to invoke this complicated hypothesis as long as the more straightforward explanation (synchrotron radiation from the region of the CD surface) seems viable.

Finally, we should explain the fact that the outer tails are not truly symmetric with respect to the trajectory of Geminga on the sky, neither in shape (especially close to the pulsar) nor, particularly, in brightness (the S-tail is considerably brighter). We could tentatively ascribe this asymmetry to nonuniform conditions (density and/or temperature) in the ambient medium. The nonuniformity is supported by the Very Large Array (VLA) and Effelsberg radio telescope HI (21 cm line) observations of the Geminga field (Giacani et al. 2005). These observations have shown the pulsar and its X-ray PWN to be in a local minimum of the HI emission, surrounded by an open HI shell (an incomplete ring with an average radius of $9'$) that envelopes the southern part of the X-ray PWN, with the internal border of the shell close to the S-tail. The lack of neutral hydrogen in the vicinity of the pulsar can be explained by the ionization caused by the pulsar's UV and soft X-ray emission. The openness of the shell (no HI emission northwest of the X-ray PWN) might imply a higher temperature (and perhaps a lower density) of the ISM in that direction. One may speculate that Geminga is crossing a cold ISM cloud and is now approaching the cloud's northwest boundary. It remains to be understood, however, how the relative brightness of the S-tail is connected with the alleged lower temperature and higher density in that region. We should also mention that, based on the HI radio results, one could expect an H_α PWN south of the S-tail, associated with the FS. However, C+03 report the nondetection of ‘‘organized diffuse H_α emission from the X-ray structure surrounding Geminga’’ in a 5 hour observation with the VLT-ANTU telescope. Their Figure 2 shows an apparent filament at the outer border of the S-tail, but it is not immediately clear whether or not this feature is related to the PWN.

To conclude, if the outer tails represent the limb-

brightened boundaries of the sky projection of a shell, this shell is most likely the synchrotron radiation from the region of interaction of the shocked PW and shocked ISM material, where the wind flow is decelerated to non-relativistic velocities by the shear instability, which implies mass loading. The shape of the shell is somewhat different from the shape of the CD surface in the available numerical PWN models, perhaps because the models do not include the mass loading and proper anisotropy of the unshocked PW.

3.1.2. *The outer tails are bent polar outflows?*

The hypothesis that the outer “tails” represent the boundary of a shell is not the only possible explanation. In particular, as no emission is seen between the outer tails except for the A-tail (see §2.2.2), we cannot exclude the possibility that the outer tails are in fact some collimated flows emanating from the pulsar magnetosphere, such as two jets aligned with the pulsar’s spin axis near the pulsar and bent by the ram pressure at larger distances. This interpretation implies a large angle Θ between the spin axis and pulsar’s velocity ($\Theta \gtrsim 60^\circ\text{--}70^\circ$, as follows from Figs. 2 and 3) and a sufficiently large angle ζ between the spin axis and the line of sight⁹.

Chandra observations have shown that jets emanating along the spin axes are ubiquitous among young PWNe (see, e.g., Weisskopf et al. 2000; Pavlov et al. 2003), and the spin axis is often approximately aligned with the pulsar velocity direction (Ng & Romani 2007). The mechanisms of jet formation and collimation are currently not certain. In the scenario discussed by Benford (1984), a fraction of electrons created in the vacuum gaps above the magnetic poles and accelerated along the open magnetic field lines is deflected toward the spin axis and forms a beam collimated by its own toroidal magnetic field. Another mechanism of axial outflow formation has been discussed by Komissarov & Lyubarsky (2004), who assume that the outflow is originally equatorial and show that the magnetic hoop stress can stop the outflow in the surface layers of the equatorial disk and redirect it into magnetically confined polar jets.

If the pulsar were not moving with respect to the ambient medium, the jet matter would keep flowing along the spin axis until the jet is destroyed by the interaction with the medium. The ram pressure exerted onto the jets of a moving pulsar can bend the jets in the direction opposite to that of the pulsar’s motion, so that the jets are seen as two tails behind the moving pulsar¹⁰.

This scenario allows one to explain the observed asymmetry of the Geminga’s outer tails (see §2.2.2). The asymmetry can be associated with the large (but different from 90°) angle Θ between the spin axis and the pulsar’s velocity. At such an orientation the angles between the ram pressure direction and the jet matter velocity directions are acute and obtuse for the southeastern and northwestern jets, respectively, which means that bending the northwestern jet is more difficult. An additional reason for the asymmetry might be a deviation of the pulsar’s magnetic field geometry from an ideal centered

dipole, which would lead to different structures of the magnetic field at the two poles and different properties of the two jets. Different brightness of the jets, especially in the pulsar vicinity, might be caused by Doppler boosting (if the angle ζ between the spin axis and line of sight is different from 90°), but it is hard to estimate the Doppler factor and to infer the angles with the current noisy data.

As the bent polar outflow interpretation of the outer tails requires a large value of the angle Θ , while Θ is apparently small for most pulsars, this interpretation implies that the outer tails are a rare phenomenon, in agreement with PWN observations that have not shown such tails in other PWNe. It, however, remains to be understood why Θ is so different for Geminga. A theoretical study of the expected distribution of this angle using the physics of the neutron star birth is required to confirm this explanation.

3.2. *The nature of the axial tail*

The straight, patchy A-tail is seen up to $50''$ ($0.06d_{250}$ pc) from the pulsar. Its surface brightness is not only nonuniform but also variable, as we see from the comparison of the 2007 and 2004 data. Assuming a nearly isotropic emission (which, rigorously speaking, implies a nonrelativistic flow), the A-tail luminosity, $L_X \sim (1-2) \times 10^{29} d_{250}^2 \text{ erg s}^{-1}$ in the 0.3–8 keV band, is $\sim (3-6) \times 10^{-6} d_{250}^2$ of Geminga’s spin-down power \dot{E} . The A-tail luminosity is $\sim 0.03\text{--}0.06$ of the nonthermal (magnetospheric) luminosity of the Geminga pulsar in the same energy range and is a factor of 2–4 lower than the total luminosity of the outer tails.

There are three conceivable explanations of the A-tail: a jet emanating from the pulsar magnetosphere in the direction opposite to the pulsar velocity, a tail part of the bowshock-tail PWN created by the supersonic motion of the pulsar, and a Doppler-boosted image of a shell into which a fraction of the relativistic PW is directed. We will discuss these interpretations below, taking into account their connection with the above-discussed interpretations of the outer tails.

3.2.1. *The axial tail is a pulsar jet?*

The interpretation of the A-tail as a pulsar jet, suggested by P+06, is consistent with only one of the above-discussed interpretations of the outer tails, namely, the hypothesis that the outer tails represent a boundary of a shell (e.g., an equatorial outflow bent by the ram pressure). As pulsar jets emerge along the pulsar’s spin axis, and the A-tail is aligned with the pulsar’s trajectory in the sky, the jet interpretation of the A-tail implies that the spin axis is likely aligned with the pulsar’s velocity. This suggests that the “natal kick” of the Geminga pulsar was directed along the spin axis, which has important implications for the mechanisms of supernova explosion and neutron star formation (e.g., Ng & Romani 2007).

The lack of a clear (counter)jet ahead of the pulsar (see, however, the note at the end of §2.2.3) could be explained by Doppler boosting (the approaching jet is brighter than the receding counterjet, assuming the jet material flows with nearly relativistic velocities). Alternatively, the counterjet can be partially or fully destroyed by the ISM ram pressure, or the outflows in the opposite directions may be intrinsically different.

⁹ The large value of ζ supports the outer gap interpretation of Geminga’s γ -ray emission (Romani & Watters 2010).

¹⁰ A similar model has been discussed by Heinz et al. (2008) for microquasars.

As described in §2.2.1, the surface brightness is distributed nonuniformly along the A-tail, with some “blobs” seen at different positions in the images of 2004 and 2007, and a “gap” between the pulsar and the beginning of the A-tail. This means that there are regions of the enhanced magnetic field and/or higher density along the A-tail, which might be caused by discrete ejections from the magnetosphere, or they could be manifestations of some instabilities (e.g., the sausage instability, as discussed by Pavlov et al. 2003 for the outer jet of the Vela PWN) or internal shocks in the jet flow. Particularly interesting is the brightest blob C seen at the apparent end of the A-tail in the image of 2007 (see Fig. 2). Although a background K star could contribute to the blob C emission (see §2.2.1), our analysis suggests that the star’s contribution is not dominant and blob C could be associated with the jet’s termination shock. To understand the nature of the blobs, it would be important to study their evolution in a series of deep observations, which, in particular, would help estimate the flow speed in the jet.

Using the observed diameter of the alleged jet and the estimate for the energy injection rate, P+06 estimate the jet’s magnetic field: $B_{\text{jet}} \sim 100 \mu\text{G}$. For such a magnetic field the expected jet length is $l_{\text{jet}} \sim v_{\text{jet}} \tau_{\text{syn}} \sim 0.6 (v_{\text{jet}}/0.5c) (B_{\text{jet}}/100 \mu\text{G})^{-3/2}$ pc, where v_{jet} is the bulk flow velocity in the jet, and τ_{syn} is the synchrotron cooling time. The jet length estimated from the initial bright portion of the axial tail, $l_{\text{jet}} \sim 0.06 d_{250} / \sin i$ pc, is much smaller than this value unless v_{jet} is much smaller than $0.5c$ and/or $\sin i$ is small, which seems unlikely. To explain this contradiction, P+06 speculate that the jet becomes uncollimated or destroyed well before it radiates its entire internal energy. To check such speculations and test the pulsar jet interpretation, deeper observations are required.

3.2.2. *The axial tail is a shocked pulsar wind?*

A tail-like structure similar to the observed A-tail could form behind the supersonically moving pulsar due to the collimation of the shocked PW by the ram pressure (B+05; Romanova et al. 2005). For instance, if we assume that the outer tails and the possible arc ahead of the pulsar delineate the CD surface (see §3.1.1), then the A-tail might be the shocked PW immediately outside (and perhaps behind) the bullet-like TS. P+06 have shown that this interpretation is not quantitatively consistent with the available simulations of bowshock-tail PWNs, but those simulations do not take into account the intrinsic anisotropy of the PW. In addition, it would be difficult to explain the presence of the blobs and the variability of the A-tail in the framework of this interpretation. Therefore, we consider this interpretation unlikely.

If the outer tails are bent polar outflows (§3.1.2), then the ram-pressure confined shocked PW would be the only possible explanation for the A-tail. A more detailed interpretation of the A-tail would depend on the PW model. For instance, if the PW were intrinsically isotropic, then the A-tail might be interpreted as originating from the shocked PW “sheath” immediately outside the TS, and the observed width of the tail would imply the distances $R_{\text{TS,h}} \approx 3''$ and $R_{\text{CD,h}} \approx 4''$ of the TS and CD heads from the pulsar. Therefore, we would expect a bright arc (brighter than any part of the ax-

ial tail) $\approx (3''-4'') \sin i$ ahead of the pulsar. No such a bright arc is seen in the images, but this does not necessarily rule out the TS origin of the A-tail because the TS head could be closer to the pulsar and hidden within the pulsar image if the PW is anisotropic (P+06). In this interpretation, however, we have to assume that no emission is seen from the CD surface region, which looks somewhat unnatural.

In the bent polar outflow interpretation of the outer tails, one could also assume that the A-tail tail is associated with the CD-confined cylindrical region behind the (unresolved) TS. In this case, for an isotropic PW, we would expect a bright arc $\approx 1'' \sin i$ ahead of the pulsar, which can easily be hidden within the pulsar image. In the framework of this interpretation, the non-uniformity and variability of the A-tail could be explained by shear instabilities at the CD surface (cf. §3.1.1), which could also decelerate the flow, so that the blobs’ velocity would be lower than that in the jet interpretation of the A-tail. We should note, however, that in such interpretations the polar outflows are more luminous than the ram-pressure confined tail (perhaps an equatorial outflow), which has not been observed for any other pulsar.

3.2.3. *The axial tail is a Doppler-boosted shell projection?*

As we have mentioned above, the image of a shell formed by material outflowing with relativistic speeds may be strongly affected by Doppler boosting, which brightens those parts of the shell where the angle θ between the bulk flow velocity and the line of sight is the smallest. For instance, a conical shell, in which the material flows from the cone vertex at the pulsar position, would look like a straight strip¹¹ corresponding to the minimum θ . If the material flows from the head of a paraboloid-like shell (e.g., the CD surface), the observer would see a shorter strip, detached from the paraboloid head in general case. In principle, one could imagine that the A-tail is such a projection of the shell formed by the shocked PW that flows out with relativistic velocities between the TS and CD, while the outer tails are bent polar outflows (jets). In this interpretation, the true transverse radius of the shell would be larger than the observed width of the A-tail. The blobs in the A-tail might be some local instabilities in the relativistic flow, which would likely move with relativistic bulk-flow velocities. Therefore, it would be important to examine the blob motion in future observations.

4. SUMMARY

The new *Chandra* and *XMM-Newton* observations of the Geminga PWN have confirmed that it has three tail-like components, unlike any other detected PWN. The new observations have allowed us to image the tails at larger distances from the pulsar and establish their patchy structure. Comparing the new and previous *Chandra* observations, we have found indications of PWN variability, especially in the axial tail and the emission ahead of the pulsar. In particular, we found up to

¹¹ A similar model has been discussed by Radhakrishnan & Deshpande (2001) who interpret the “inner jets” of the Vela PWN as a projection of the rotating beams of relativistic particles emitted along the magnetic axes.

three blobs in the axial tail, at different positions in 2004 and 2007.

Similar to other X-ray PWNe, the Geminga PWN is due to synchrotron radiation of shocked PW comprised of relativistic particles. Based on the new and old observations, we have proposed several competing interpretations of the PWN structure. Very likely, the outer tails delineate a limb-brightened boundary of a shell-like region of interaction of the shocked PW and shocked ISM, while the axial tail is a pulsar jet along the spin axis aligned with the pulsar's trajectory. Such an interpretation implies a nonrelativistic speed of the bulk outflow along the shell, possibly decelerated by the shear instability and mass loading. Alternatively, the outer tails could be polar outflows from the pulsar magnetosphere (e.g., pulsar jets along the spin axis), bent by the ISM ram pressure, in which case the axial tail could be a shocked PW (e.g., an equatorial outflow) collimated by the ISM ram pressure exerted on the supersonically moving PWN.

To discriminate between various interpretation of the observed PWN, a series of carefully designed *Chandra* observations is required. In particular, such observations should allow one to measure the speeds of the bulk flows in the tails, which would distinguish fast jets from ram-pressure-confined pulsar winds slowed down by the in-

teraction with the ambient ISM. Also, such observations should be deep enough to establish the true morphology of the emission in the immediate vicinity of the pulsar. For instance, if a deeper observation convincingly shows that there is an arc ahead of the pulsar connecting the two outer tails, then the bending axial outflows scenario will be ruled out. If, however, we see two straight tails originating from the pulsar in a direction inclined to the pulsar's velocity direction, then the tails can be interpreted as bent jets. In addition, the detailed modeling of anisotropic magnetic PW from a high-speed pulsar will also be extremely useful to properly interpret the observational data.

We thank Andrew Melatos for useful discussions of the PWN modeling. Support for this work was provided by the National Aeronautics and Space Administration through *Chandra* Award Number GO7-8053A issued by the *Chandra* X-ray Observatory Center, which is operated by the Smithsonian Astrophysical Observatory for and on behalf of the National Aeronautics Space Administration under contract NAS8-03060. The work by GGP was also partially supported by NASA grant NNX09AC84G.

REFERENCES

- [Benford, G. 1984, ApJ, 282, 154
 [Bertsch, D. L., et al. 1992, Nature, 357, 306
 [Bignami, G. F., Caraveo, P. A., & Paul, J. A. 1988, A&A, 202, L1
 [Bucciantini, N. 2002, A&A, 387, 1066
 [Bucciantini, N., Amato, E., & Del Zanna, L. 2005, A&A, 434, 189 (B+05)
 [Caraveo, P. A., Bignami, G. F., de Luca, A., Mereghetti, S., Tur, A., & Becker, W. 2003, Science, 301, 1345 (C+03)
 [Cutri, R. M., et al. 2003, The IRSA 2MASS All-Sky Point Source Catalog, NASA/IPAC Infrared Source Archive (Pasadena, CA: CalTech), <http://irsa.ipac.caltech.edu/applications/Gator/>
 [de Luca, A., Caraveo, P. A., Mereghetti, S., Negroni, M., & Bignami, G. F. 2005, ApJ, 623, 1051
 [de Luca, A., Caraveo, P. A., Mattana, F., Pellizzoni, A., & Bignami, G. F. 2006, A&A, 445, L9
 [Faherty, J., Walter, F. M., & Anderson, J. 2007, Ap&SS, 308, 225
 [Gaensler, B. M., et al. 2004, ApJ, 616, 383
 [Gaensler, B. M., & Slane, P. O. 2006, ARA&A, 44, 17
 [Giacani, E., Reynoso, E., Dubner, G., Goss, W. M., Green, A., & Johnston, S. 2005, Adv. Space Res., 35, 1070
 [Halpern, J. P., & Holt, S. S. 1992, Nature, 357, 222
 [Halpern, J. P., & Tytler, D. 1988, ApJ, 330, 201
 [Heinz, S., Grimm, H. J., Sunyaev, R. A., & Fender, R. P. 2008, ApJ, 686, 1145
 [Kargaltsev, O., & Pavlov, G. G. 2008, in AIP Conf. Proc. 983, 40 Years of Pulsars: Millisecond Pulsars, Magnetars, and More, ed. C. Bassa, A. Cumming, V. M. Kaspi, & Z. Wang (Melville, NY: AIP), 171 (KP08)
 [Kargaltsev, O., Pavlov, G. G., & Garmire, G. P. 2007, ApJ, 660, 1413
 [Kargaltsev, O. Y., Pavlov, G. G., Zavlin, V. E., & Romani, R. W. 2005, ApJ, 625, 307
 [Kargaltsev, O., Misanovic, Z., Pavlov, G. G., Wong, J. A., & Garmire, J. P. 2008, ApJ, 684, 542
 [Kaspi, V. M., Roberts, S. E., & Harding, A. K. 2006, in Compact Stellar X-Ray Sources, ed. W. H. G. Lewin & M. van der Klis (Cambridge: Cambridge Univ. Press), 279
 [Komissarov, S. S., & Lyubarsky, Y. E. 2004, MNRAS, 349, 779
 [Koptsevich, A. B., Pavlov, G. G., Zharikov, S. V., Sokolov, V. V., Shibanov, Yu. A., & Kurt, V. G. 2001, A&A, 370, 1004
 [Lasker, B. M., et al. 2008, AJ, 136, 735
 [Maccacaro, T., Gioia, I. M., Wolter, A., Zamorani, G., & Stocke, J. T. 1988, ApJ, 326, 680
 [McGowan, K. E., Vestrand, W. T., Kennea, J. A., Zane, S., Cropper, M., Córdova, F. A. 2006, ApJ, 647, 1300
 [Misanovic, Z., Pavlov, G. G., & Garmire, G. P. 2008, ApJ, 685, 1129
 [Monet, D. G., et al. 2003, AJ, 125, 984
 [Ng, C.-Y., & Romani, R. W. 2007, ApJ, 660, 1357
 [Pavlov, G. G., Sanwal, D., & Zavlin, V. E. 2006, ApJ, 643, 1146 (P+06)
 [Pavlov, G. G., Teter, M. A., Kargaltsev, O., & Sanwal, D. 2003, ApJ, 591, 1157
 [Radhakrishnan, V., & Deshpande, A. A. 2001, A&A, 379, 551
 [Romani, R. W., & Watters, K. P. 2010, ApJ, 714, 810
 [Romanova, M. M., Chulsky, G. A., & Lovelace, R. V. E. 2005, ApJ, 630, 1020
 [Sanwal, D., Pavlov, G. G., & Zavlin, V. E. 2004, BAAS, 36, 923
 [Thompson, D. J., Fichtel, C. E., Hartman, R. C., Kniffen, D. A., & Lamb, R. C. 1977, ApJ, 213, 252a
 [Vigelius, M., Melatos, A., Chatterjee, S., Gaensler, B. M., & Ghavamian, P. 2007, MNRAS, 374, 793
 [Weisskopf, M. C., et al. 2000, ApJ, 536, L81
 [Weisskopf, M. C., Wu, K., Trimble, V., O'Dell, S. L., Elsner, R. F., Zavlin, V. E., Kouveliotou, C. 2007, ApJ, 657, 1026
 [Wilkin, F. P., 1996, ApJ, 459, L31
 [Zacharias, N., Monet, D. G., Levine, S. E., Urban, S. E., Gaume, R., & Wycoff, G. L. 2004, BAAS, 36, 1418

TABLE 1
 PROPERTIES OF THE PWN ELEMENTS FROM THE *Chandra* DATA OF 2007 AND 2004.

PWN element	Area ^a	Counts ^b	<i>S/N</i>	Γ	Flux ^c	Luminosity ^d
A-tail (2007; bright) ^e	705.6	82.6 ± 12.0	6.9	1.84 ^{+0.29} _{-0.26}	1.19 ^{+0.30} _{-0.32}	0.92 ^{+0.15} _{-0.12}
A-tail (2007; bright, w/o blob C) ^f	677.1	56.8 ± 10.8	5.3	1.87 ^{+0.41} _{-0.36}	0.77 ^{+0.20} _{-0.21}	0.60 ^{+0.14} _{-0.10}
A-tail (2007; faint)	2404.2	29.8 ± 17.2	1.7	-0.12 ^{+0.86} _{-1.18}	1.15 ^{+0.35} _{-1.15}	0.86 ^{+0.53} _{-0.46}
A-tail (2004)	118.1	45.6 ± 7.1	6.4	1.26 ^{+0.28} _{-0.27}	2.15 ^{+0.66} _{-0.78}	1.64 ^{+0.35} _{-0.31}
N-tail (2007; bright)	462.3	39.4 ± 8.8	4.5	-0.11 ^{+0.49} _{-0.58}	1.21 ^{+0.25} _{-0.41}	0.91 ^{+0.32} _{-0.24}
N-tail (2007; faint)	4011.9	52.9 ± 24.3	2.2	0.82 ^{+0.60} _{-0.57}	1.30 ^{+0.64} _{-1.07}	0.98 ^{+0.50} _{-0.43}
N-tail (2007; entire)	4474.2	92.3 ± 26.9	3.4	0.47 ^{+0.49} _{-0.53}	2.33 ^{+0.63} _{-1.45}	1.76 ^{+0.64} _{-0.63}
S-tail (2007; bright)	2258.0	139.0 ± 19.6	7.1	1.17 ^{+0.27} _{-0.25}	2.58 ^{+0.42} _{-0.50}	1.96 ^{+0.38} _{-0.34}
S-tail (2007; faint)	3740.7	28.8 ± 22.7	1.3	1.82 ^{+0.50} _{-0.46}	1.03 ^{+0.48} _{-0.36}	0.80 ^{+0.26} _{-0.22}
S-tail (2007; entire)	5998.7	167.8 ± 33.8	5.0	1.59 ^{+0.30} _{-0.28}	3.21 ^{+0.72} _{-0.70}	2.47 ^{+0.46} _{-0.38}
S-tail (2004)	985.3	33.0 ± 9.0	3.7	1.20 ^{+0.45} _{-0.42}	1.58 ^{+0.53} _{-0.57}	1.20 ^{+0.49} _{-0.38}
Arc (2007)	86.6	16.3 ± 4.8	3.4	1.07 ^{+0.73} _{-0.67}	0.25 ^{+0.19} _{-0.06}	0.19 ^{+0.10} _{-0.07}
Arc (2004)	86.6	22.8 ± 5.1	4.5	0.90 ^{+0.46} _{-0.43}	1.19 ^{+0.51} _{-0.83}	0.90 ^{+0.39} _{-0.28}

NOTE. — The initial bright and extended faint portions of the three PWN tails in the data of 2007 are shown in Fig. 3. The A-tail, N-tail, and S-tail stand for the axial tail, the northern tail, and the southern tail, respectively. The spectra of the PWN elements were fitted with the absorbed power-law model (photon index Γ) at a fixed hydrogen column density $N_{\text{H}} = 1.1 \times 10^{20} \text{ cm}^{-2}$. The errors are given at the 1σ level, for one interesting parameter.

^aArea of the PWN element in arcsec².

^bBackground-subtracted counts in PWN elements.

^cObserved (absorbed) flux in the 0.3–8 keV band, in units of $10^{-14} \text{ erg cm}^{-2} \text{ s}^{-1}$, estimated with XSPEC.

^dUnabsorbed luminosity in the 0.3–8 keV band, assuming isotropic emission and distance of 250 pc, in units of $10^{29} \text{ erg s}^{-1}$.

^eBlob C at the end of the brighter portion of the axial tail is included.

^f Blob C (3'' radius) is excluded from the data.

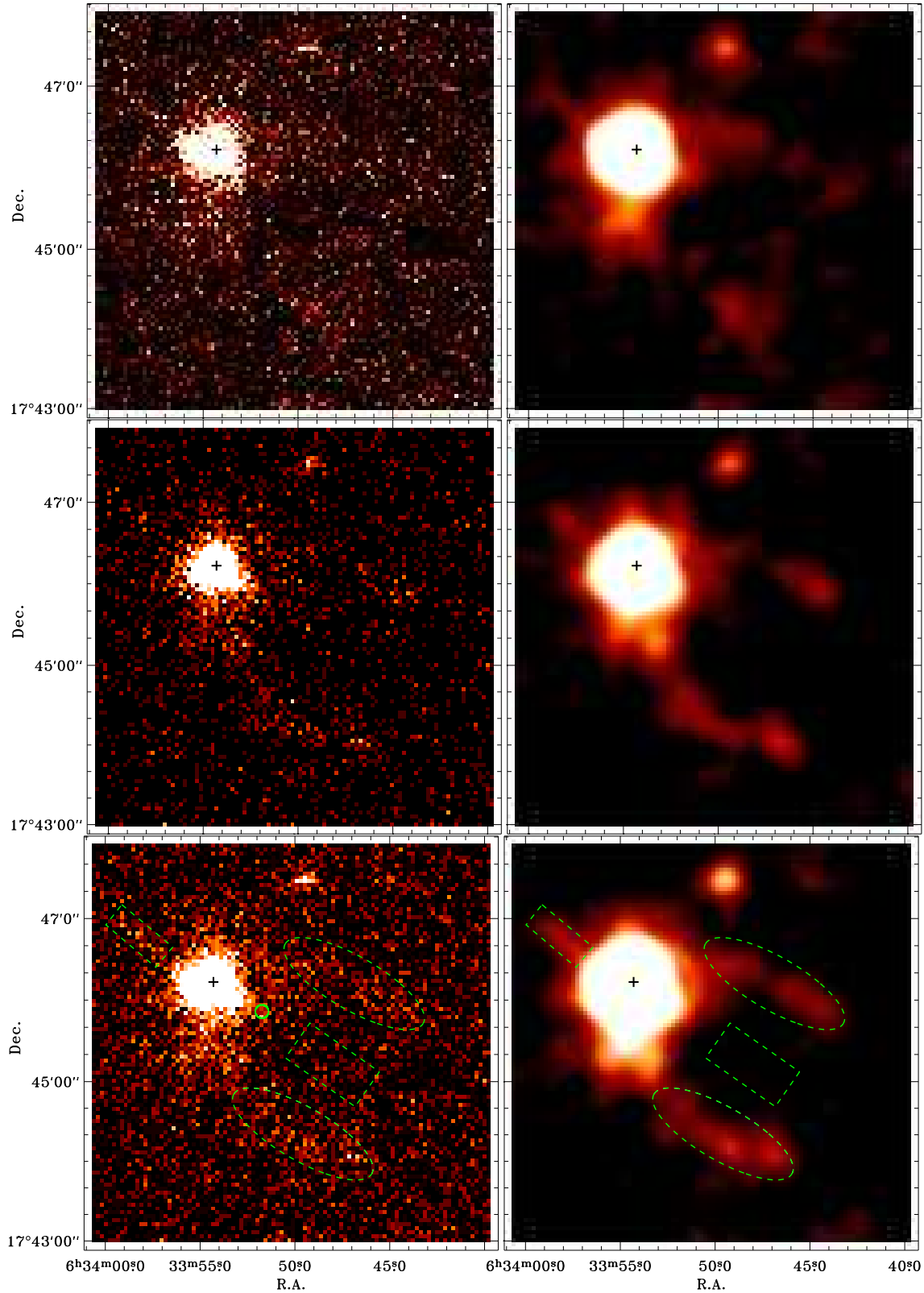


FIG. 1.— XMM-Newton MOS1+MOS2 images ($5' \times 5'$) of the Geminga pulsar and its PWN in the 0.5–8 keV band. The top, middle and bottom panels correspond to the observation of 2004–2007 (64 ks total scientific exposure), 2002 (78 ks), and 2002–2007 (142 ks), respectively. The images in the left panels are binned in $3'' \times 3''$ pixels, while the images in the right panels are additionally smoothed with a $18''$ FWHM Gaussian. The ellipses ($120'' \times 40''$) show the regions for which the spectra and fluxes were measured, while the $64'' \times 32''$ rectangle between the ellipses was used for estimating the upper limit on the surface brightness between the outer tails (see § 2.2.2). The $50'' \times 20''$ rectangle ahead of the pulsar was used to measure the spectrum of the “streak” (see § 2.2.3). The $5''$ radius circle in the bottom left panel is centered at the position of blob C found in the *Chandra* observation of 2007 (see Fig. 2 and § 2.2.1). The source north-northwest of the pulsar is an 11-th magnitude K star (C+03).

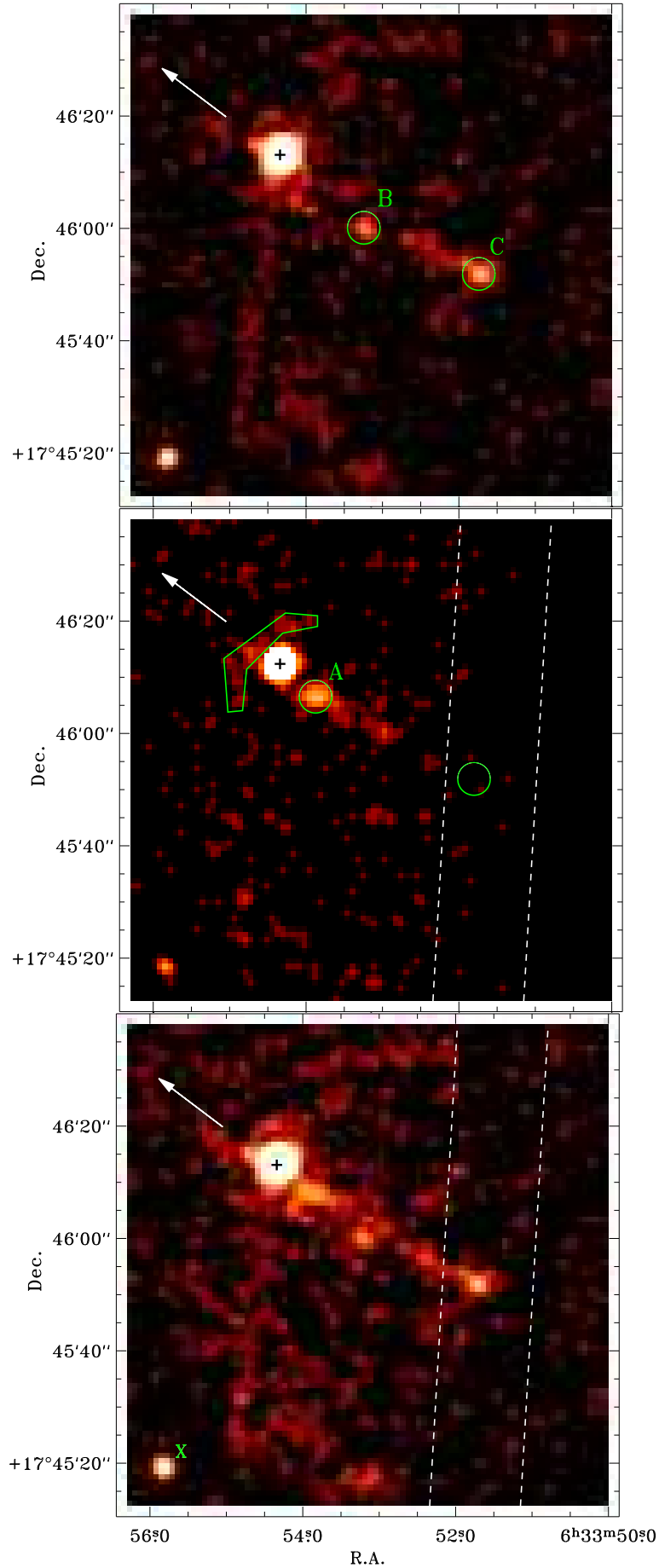


FIG. 2.— $1'6 \times 1'6$ images of the Geminga pulsar and its PWN from the *Chandra* observations of 2007 and 2004 (top and middle panels, respectively), and the combined image (bottom), in the 0.3–8 keV range. The original data were binned in $1'' \times 1''$ pixels and smoothed with a $2''$ FWHM Gaussian. The arrows show the pulsar's proper motion, whereas the dashed lines in the middle and bottom panels indicate the sky region for which the exposure was reduced by the telescope dithering (from 18.8 to 0 ks, in the 2004 observation). Three

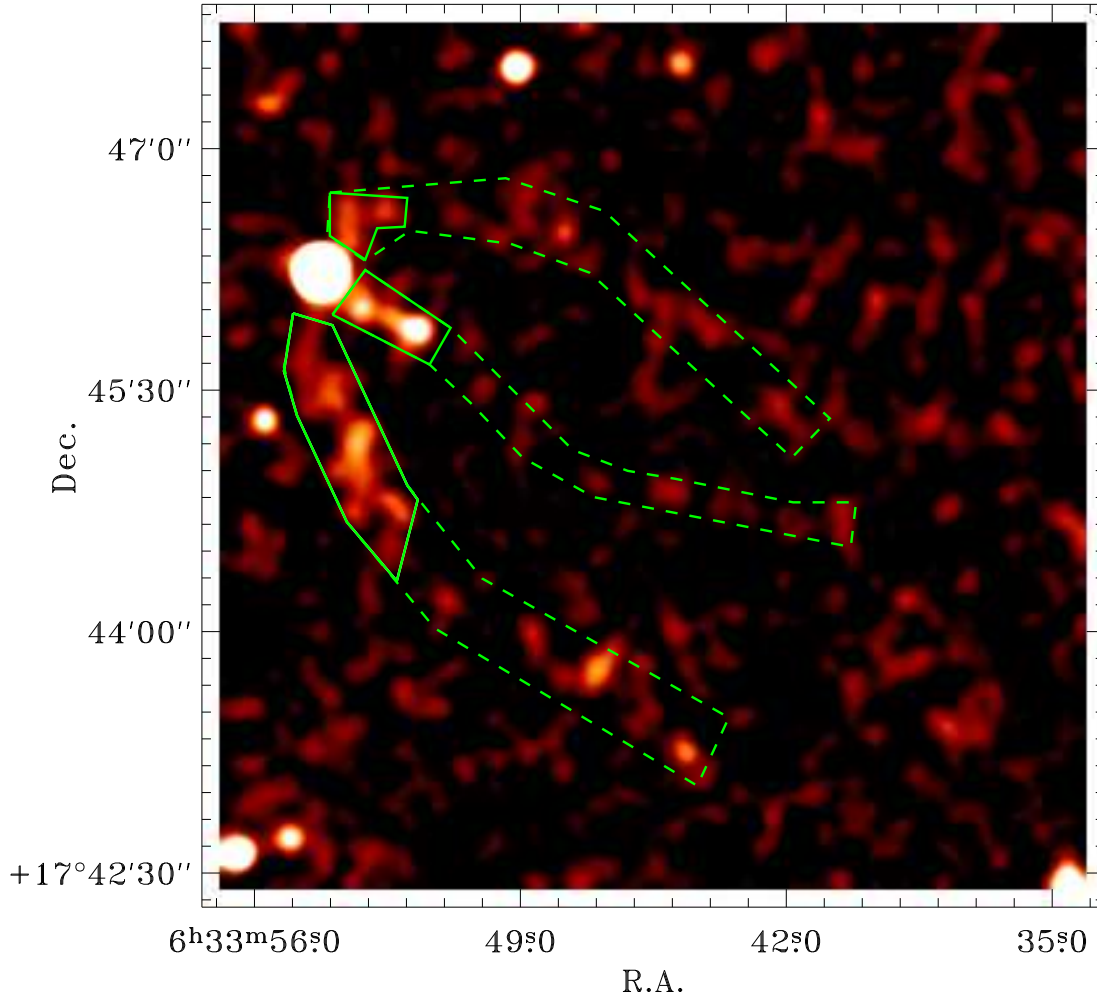


FIG. 3.— $5.4' \times 5.4'$ image of the Geminga PWN in the *Chandra* data of 2007. The solid and dashed contours show the regions used for extracting the spectra of brighter and fainter parts of the PWN tails, respectively.

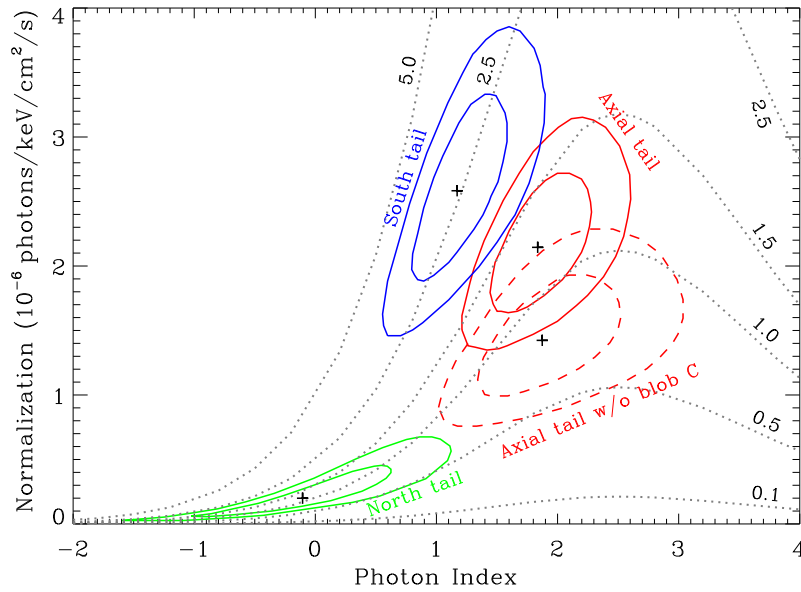


FIG. 4.— Confidence contours for the PL normalization versus photon index (at the 68.3% and 95.4% levels, for two interesting parameters) for bright portions of the PWN tails from the *Chandra* 2007 data. The hydrogen column density is fixed at $N_{\text{H}} = 1.1 \times 10^{20} \text{ cm}^{-2}$. The dotted curves correspond to constant unabsorbed flux values (depicted near the curves, in units of $10^{-14} \text{ erg cm}^{-2} \text{ s}^{-1}$).

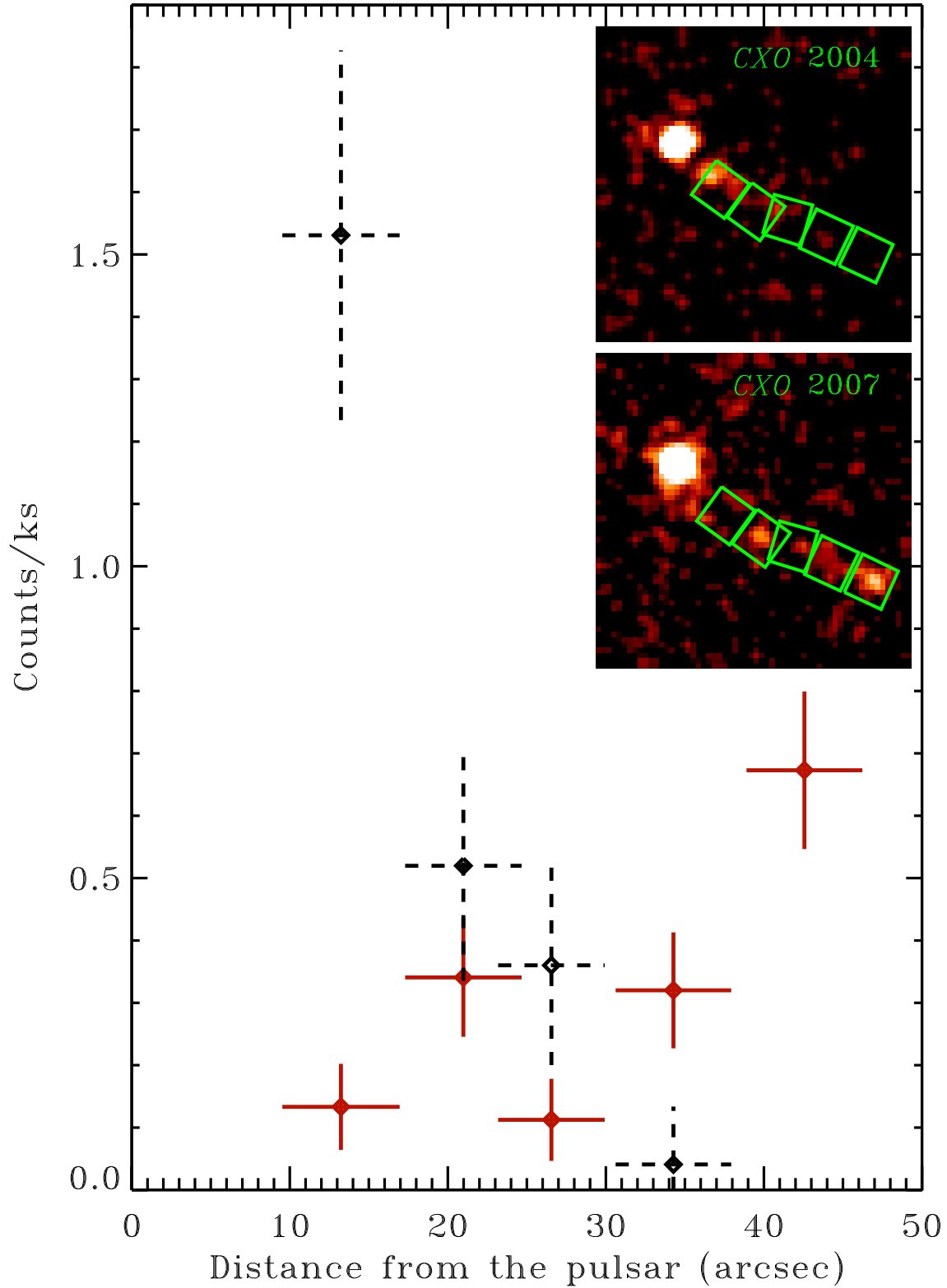


FIG. 5.— Count rate profiles along the axial tail in the *Chandra* data. The net count rates are calculated in square boxes of equal size (59.5 arcsec^2), shown in the inset. The dashed (black) and solid (red) points (with 1σ errors) are for the 2004 and 2007 data, respectively. The count rates and their errors for the 2007 data are multiplied by a factor of 1.6 to account for the different sensitivities of the I3 and S3 chips.

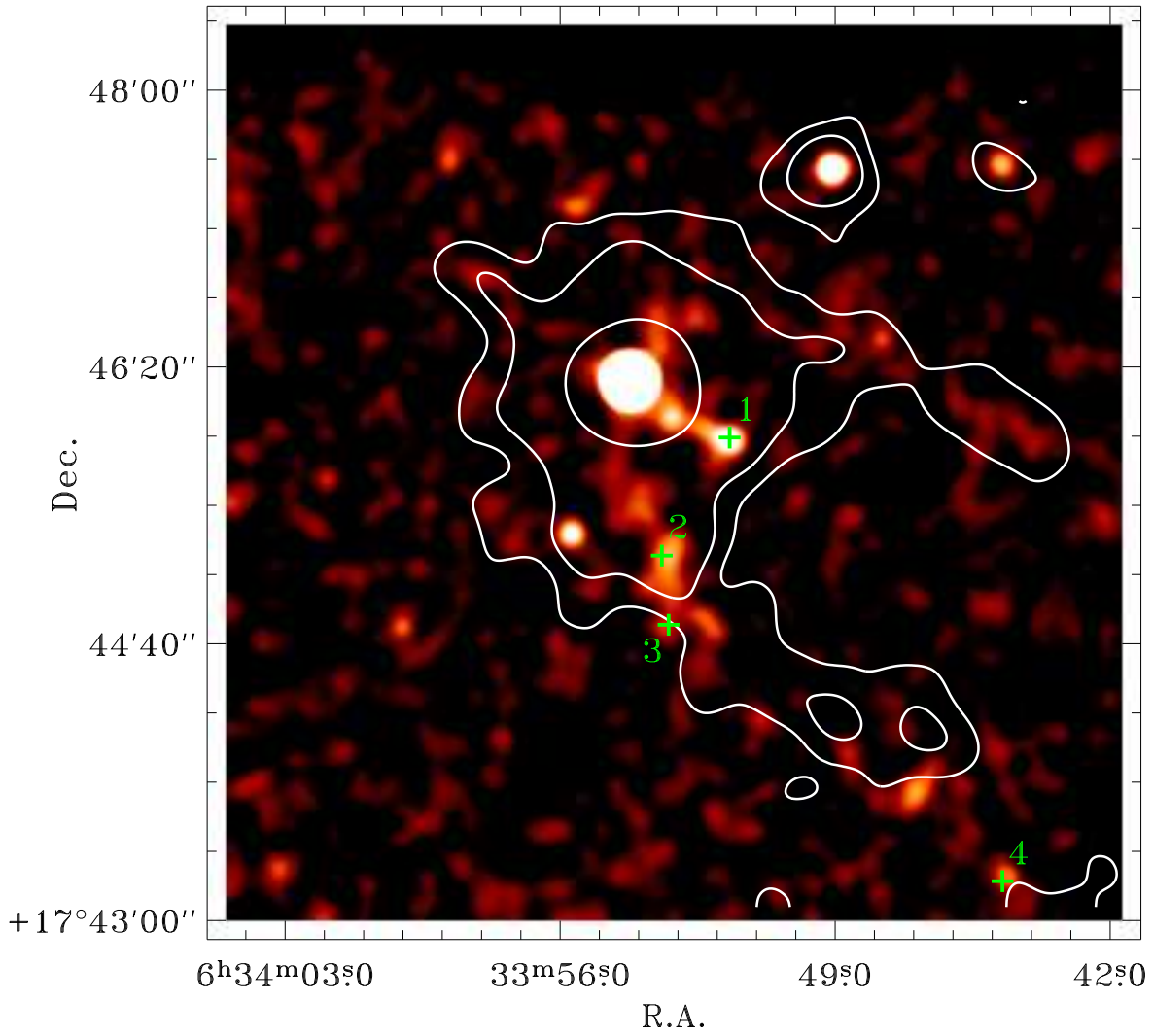


FIG. 6.— $5'4 \times 5'4$ image of the Geminga pulsar and its PWN from the *Chandra* data of 2007 binned in $1'' \times 1''$ pixels and smoothed with an $8''$ FWHM Gaussian, with overlaid brightness contours from the *XMM-Newton* image shown in Fig. 1. The green crosses with numbers indicate the positions of optical stars projected onto the PWN elements.